

*Suzaku* OBSERVATION OF GRS 1915+105:  
EVOLUTION OF ACCRETION DISC STRUCTURE DURING LIMIT-CYCLE OSCILLATION

Y. UEDA<sup>1</sup>, K. HONDA<sup>2</sup>, H. TAKAHASHI<sup>2</sup>, C. DONE<sup>3</sup>,  
H. SHIRAI<sup>2</sup>, Y. FUKAZAWA<sup>2</sup>, K. YAMAOKA<sup>4</sup>, S. NAIK<sup>5</sup>,  
H. AWAKI<sup>6</sup>, K. EBISAWA<sup>7</sup>, J. RODRIGUEZ<sup>8</sup>, S. CHATY<sup>8</sup>

*Draft version March 23, 2022*

ABSTRACT

We present results from the *Suzaku* observation of the microquasar GRS 1915+105 performed during the 2005 October multiwavelength campaign. The data include both stable state (class  $\chi$ ) and limit-cycle oscillation (class  $\theta$ ). Correct interstellar absorption as well as effects of dust scattering are fully taken into account in the spectral analysis. The energy spectra in the 2–120 keV band in both states are all dominated by strong Comptonization of disk photons by an optically thick ( $\tau \approx 7$ –10) and low temperature ( $T_e \approx 2$ –3 keV) hybrid plasmas containing non-thermal electrons produced with 10–60% of the total power input. Absorption lines of highly ionized Fe ions detected during the oscillation indicate that a strong disk wind is developed. The ionization stage of the wind correlates with the X-ray flux, supporting the photoionization origin. The iron-K emission line shows a strong variability during the oscillation; the reflection is strongest during the dip but disappears during the flare. We interpret this as evidence for “self-shielding” that the Comptonizing corona becomes geometrically thick in the flare phase, preventing photons from irradiating the outer disk. The low-temperature and high luminosity disk emission suggests that the disk structure is similar to that in the very high state of canonical black hole binaries. The spectral variability during the oscillation is explained by the change of the disk geometry and of the physical parameters of Comptonizing corona, particularly the fractional power supplied to the acceleration of non-thermal particles.

*Subject headings:* accretion, accretion disks — stars: individual (GRS 1915+105) — techniques: spectroscopic — X-rays: stars

1. INTRODUCTION

GRS 1915+105 is the brightest microquasar in our Galaxy, providing us with a unique opportunity to study the accretion flow onto a black hole at high fractions of Eddington ratio (for a review, see Fender & Belloni 2004). This source, discovered in 1992 with the WATCH instrument on GRANAT (Castro-Tirado et al. 1992), has been persistently active up to now unlike usual soft X-ray transients. GRS 1915+105 was recognized to be a superluminal source by VLBA observations of radio outbursts (Mirabel & Rodríguez 1994), making it a target of great importance for studying the formation mechanism of relativistic jets. From the kinetics of the radio jets, their intrinsic speed and inclination are determined to be  $0.92c$ – $0.98c$  ( $c$  is the light speed) and  $66^\circ$ – $70^\circ$ , respectively (Mirabel & Rodríguez 1994; Fender et al. 1999). The near infrared observations have revealed that the system consists of a black hole with a mass of  $14 \pm 4 M_\odot$  and a K III type companion star with an orbital period of 33.5

days (Greiner, Cuby, & McLaughran 2001). This indicates a huge size of the accretion disk with a continuously high mass transfer rate from the companion, which may account for many unique features of this source compared with normal black hole binary systems.

The source has been intensively studied at high energies by many observatories on different occasions. *RXTE*/PCA observations revealed that GRS 1915+105 often exhibits dramatic temporal and spectral variations, so-called limit-cycle oscillations, unique features in accreting stellar mass black holes in our Galaxy (e.g., Belloni et al. 1997a). Belloni et al. (2000) found the instantaneous spectral state of GRS 1915+105 can be divided into states, States A, B, and C, where the source undergoes frequent transition or stays stable. Based on these transition patterns, they classified them into 12 Classes, including 2 “stable” classes (Class  $\chi$  and  $\phi$ ) with little variability on a time scale longer than  $\sim 1$  sec. This behavior is quite different from normal black holes observed in canonical states, the low/hard, intermediate (or very high), and high/soft states (Tanaka & Lewin (1995); see also Homan & Belloni (2005) and Remillard & McClintock (2006) for more recent classification). The correspondence of States A, B, and C of

<sup>1</sup> Department of Astronomy, Kyoto University, Kyoto 606-8502, Japan

<sup>2</sup> Department of Physical Science, Hiroshima University, Hiroshima 739-8526, Japan

<sup>3</sup> Department of Physics, University of Durham, South Road, Durham, UK

cle behaviors of GRS 1915+105 qualitatively (Ohsuga 2006). However, direct observations that trace the evolution of the disk structure both in the oscillation and stable state are still insufficient to be compared with model predictions, and their interpretations may be subject to large uncertainties since understanding of the origin of the X-ray emission is not fully established. Many early works relied on the spectral modelling by a multi-color disk (MCD; Mitsuda et al. 1984) model plus a power law, as applied to other black hole binaries. There is no guarantee that this model always holds to GRS 1915+105, in particular when the power law component dominates the entire flux.

Later observational works (Zdziarski et al. 2001; Done et al. 2004; Ueda et al. 2009) have suggested that the X-ray spectra of GRS 1915+105 at least in some states are dominated by an optically-thick Comptonization of the disk photons off low energy electrons, by applying physically more realistic models than the canonical MCD + power law model. Zdziarski et al. (2001, 2005) analyzed broad band spectra observed with *RXTE*/PCA, HEXTE, and *CGRO*/OSSE, and found that they can be described by Comptonization from thermal/non-thermal hybrid plasmas. Such low temperature, optically-thick Comptonization may be common characteristics in accretion flows at high Eddington fractions, which may apply to those onto supermassive black holes (Middleton et al. 2009).

Observations of local spectral features such as iron-K emission line and absorption lines give key information to reveal the structure of accretion disks. From high resolution spectra (CCD or the HETGS instrument on *Chandra*) of GRS 1915+105, absorption lines from highly ionized ions have been clearly detected (Kotani et al. 2000; Lee et al. 2002; Ueda et al. 2009). This indicates the presence of strong disk wind most probably occurring at  $r \sim 10^5 r_g$  ( $r_g \equiv GM/c^2$  is the gravitational radius where  $G$ ,  $M$ , and  $c$  being the gravitational constant, mass of the black hole, and light velocity, respectively), which carries a huge amount of accreting gas outward the system (Ueda et al. 2009; Neilsen & Lee 2009). On the other hand, the emission line profile gives constraints on the geometry between the continuum emitting region and reflector, most probably the accretion disk. An iron-K emission line has been detected from GRS 1915+105, whose shape and intensity seem to depend on the states (Kotani et al. 2000; Neilsen & Lee 2009). Since its equivalent width is not large ( $< 50$  eV) in GRS 1915+105, we need both good spectral resolution and large effective area to accurately measure the profile, in particular to trace the change during oscillations.

*Suzaku* (Mitsuda et al. 2007), the 5th Japanese X-ray satellite, observed GRS 1915+105 on 2005 October 16–18 (UT throughout the paper) as a part of the science working group’s observation program. The large effective area with good energy resolution in the 0.2–12 keV band, together with the simultaneous coverage of the 10–600 keV band with unprece-

light curves and states of GRS 1915+105 in our observations. The spectral analysis is presented in § 4. We discuss the interpretation of our results in § 5. The conclusions are summarized in § 6. In our paper, we assume the distance of  $D = 12.5$  kpc and inclination angle of  $i = 70^\circ$  unless otherwise stated. Around the epoch of our *Suzaku* observations, a large multiwavelength campaign was conducted involving other space and ground observatories, whose results will be reported in a separate paper (Ueda et al., in preparation). For the preliminary results of the campaign, refer to Ueda et al. (2006). The *INTEGRAL* light curves are published in Rodriguez et al. (2008a).

## 2. OBSERVATIONS AND DATA REDUCTION

*Suzaku* observed GRS 1915+105 from 2005 Oct 16 16:42 to Oct 18 23:16 for a net exposure of  $\approx 80$  ksec. *Suzaku* carries four sets of X-ray Telescope (XRT) each with a focal plane X-ray CCD camera, the X-ray Imaging Spectrometer (Front-side Illuminated XISs, XIS-0, XIS-2, and XIS-3; Back-side Illuminated XIS, XIS-1), and a non-imaging collimated instrument called the Hard X-ray Detector (HXD), which consists of the silicon  $p$ -intrinsic- $n$  photo-diodes (PIN) and scintillation counters made of gadolinium silicate crystals (Ce-doped  $Gd_2SiO_5$ ; GSO). The XIS, PIN, and GSO simultaneously covers the energy band of 0.2–12 keV, 10–60 keV, and 40–600 keV, respectively. The target was observed at the so-called XIS-nominal position.

The XISs were operated in the normal clock mode with the  $2 \times 2$  editing mode for XIS-0, 2, and 3, and  $3 \times 3$  for XIS-1. To minimize pile-up (double photon events) due to the brightness of this source, the 1/8 window option was adopted for XIS-0, XIS-2, and XIS-3, which reduced the exposure time per frame from 8 sec to 1 sec. XIS-1 was operated with the 0.1 sec burst plus 1/8 window option, although the 1/8 window option was turned off for XIS-1 before Oct 18 00:26, due to an accidental error in the satellite operation. We utilize XIS data taken with different modes according to the purpose of an analysis. The XIS-1 events are used to derive (1) unsaturated light curves with a resolution of 1 sec (after Oct 18 00:26) and 8 sec (before then) and (2) continuum spectra with little effects from pile-up, while we use XIS-0, 2 and 3 data to make the spectra with high photon statistics in the 5–10 keV band for detailed study of the iron-K features.

We analyze the data using the HEASoft version 6.4.1 package, utilizing the products version 2.0.6.13 processed by the pipeline processing team and calibration database (CALDB) released on 2008 Dec. 3. For the analysis of the XIS data, we exclude events suffering from telemetry saturation, based on the GTI filters provided by the XIS team<sup>9</sup>. We do not subtract the non X-ray background nor the cosmic X-ray background, which are negligible compared with the bright source counts. For the spectral analysis of the XIS-1 data taken with the full window mode before Oct 18 00:26, we subtract out-of-time

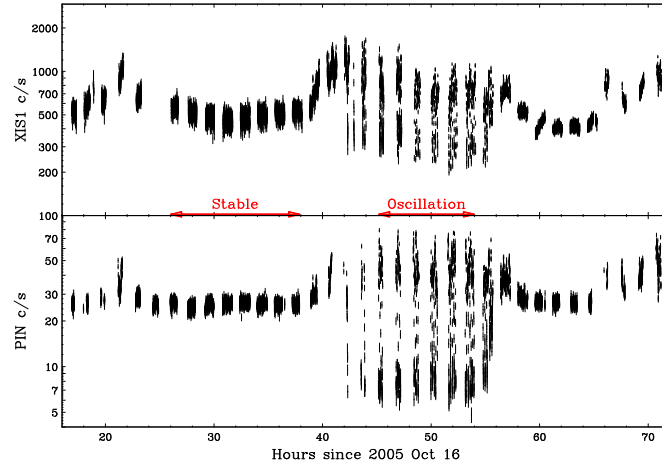


FIG. 1.— The light curves of GRS 1915+105 in the 1–10 keV and 10–60 keV band obtained with XIS-1 and HXD/PIN, respectively. The data are binned in intervals of 16 seconds. The red arrows denote the time regions used for the spectral analysis of the stable and oscillation states.

onds.

For the HXD, we use the best modelled background files provided by the HXD team<sup>10</sup>. The reproducibility of the NXB spectra with a 10 ksec exposure is known to be 1.4% and 0.6% for the PIN (15–40 keV) and GSO (50–100 keV), respectively (Fukazawa et al. 2009). Then, an estimated CXB spectrum is added to the NXB spectrum of the PIN with the angular transmission function for a uniformly extended emission. The CXB is neglected in analysis of the GSO data.

### 3. LIGHT CURVES AND X-RAY STATES

Figure 1 shows the light curves of GRS 1915+105 obtained with XIS-1 in the 1–10 keV band and with the HXD/PIN in the 10–60 keV during the whole observation epoch. All photons observed in the XIS-1 chip are utilized here, but the XIS-1 count rates before Oct 18 00:26 are artificially reduced by a factor of 0.51 to correct for the difference of the integration area from the data taken with the 1/8 window option. For convenience, hereafter we define  $t$  as the time since 2005 October 16.0 in units of hours. It is seen that at  $t \lesssim 40$  GRS 1915+105 was in an X-ray stable state, except for a possible flare-like event seen at  $t \simeq 21.5$ . From  $t \simeq 40$ , the X-ray flux increased rapidly and entered into “oscillation” that lasted till  $t \simeq 56$ . From  $t \simeq 66$ , GRS 1915+105 exhibits a similar X-ray flare, followed by oscillation whose variability pattern is different from the previous one (see Ueda et al. 2006 and Rodriguez et al. 2008a for X-ray light curves observed with other satellites). Throughout the observation, the source was very bright in soft X rays,  $\sim (1-3) \times 10^{-8}$  erg cm<sup>-2</sup> s<sup>-1</sup> in the 2–10 keV band.

For comparison with previous studies of GRS 1915+105 we first identify the “Class” and “State” of GRS 1915+105 in

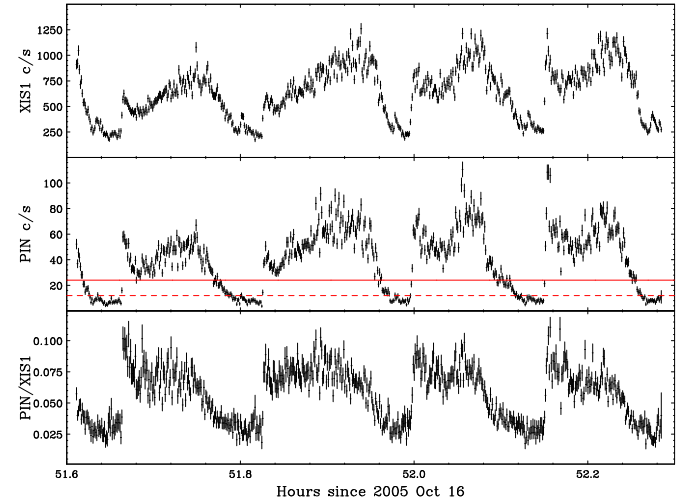


FIG. 2.— A blow up of XIS-1 (1–10 keV) and PIN (10–60 keV) light curves at  $t = 51.6-52.3$  and their hardness ratio with 4 sec bin. The two horizontal lines indicate the limits between the oscillation low/med and med/high states, respectively.

to Class  $\chi$  (stable State C) having an extremely soft spectrum, accompanied with a quasi periodic oscillation (QPO) at  $\approx 6$  Hz (Ueda et al. 2006).

Figure 2 shows representative X-ray light curves ( $t = 51.6-52.3$ ) in the oscillation phase taken with *Suzaku* XIS-1 and PIN in the 1–10 keV and 10–60 keV band, respectively, together with their hardness ratio. We identify the X-ray variability pattern as Class  $\theta$  in Belloni et al. (2000), where the transition occurs between State C and State A (soft dip) on a time scale of  $\sim 10$  minutes. It is seen that during oscillations the spectral colors significantly softens in the dip phase, as expected according to previous studies with *RXTE* (Belloni et al. 2000).

## 4. SPECTRAL ANALYSIS

### 4.1. Overview

For spectral analysis, we define four different states (a) “stable state” (Stable), (b) “oscillation high state” (Osc-H), (c) “oscillation medium state” (Osc-M), and (d) “oscillation low state” (Osc-L), according to time variability pattern and intensity level. The stable and oscillation-high states consist of State C data defined by Belloni et al. (2000), while oscillation-med and low corresponds to State A. The time region is taken between  $t = 26.03-37.88$  for (a), when the source flux was almost constant (Class  $\chi$ ), and  $t = 45.18-53.97$  for the rest (Class  $\theta$ ). The oscillation high, med, low states are defined as when the 10–60 keV PIN count rate is above 24 c s<sup>-1</sup>, between 12–24 c s<sup>-1</sup>, and between 1–12 c s<sup>-1</sup>, respectively, within the above time region. The count rate thresholds for the oscillation states are illustrated by two lines

TABLE 1  
STATE DEFINITION

State	Start (UT)	End (UT)	Criteria PIN (10–60 keV)	Exposure (ksec)
Stable	2005 Oct. 17 02:02	Oct. 17 13:53	...	19.8
Osc-H	2005 Oct. 17 21:11	Oct. 18 05:58	>24 c/s	7.2
Osc-M	2005 Oct. 17 21:11	Oct. 18 05:58	12–24 c/s	0.93
Osc-L	2005 Oct. 17 21:11	Oct. 18 05:58	1–12 c/s	2.6

used for each purpose. For the former step, we use XIS-0, 2, and 3 (FI-XISs), which were operated without the burst options, by excluding the central core of the point spread functions; this makes us achieve good photon statistics by avoiding extreme pile-up effects. The spectra of the three sensors are summed together with the energy responses. For the latter step, we make a simultaneous spectral fit to the spectra of XIS-1 (BI-XIS), PIN, and GSO, covering the 2–120 keV band, for the stable and oscillation-high states, while we only use the XIS and PIN spectra in the 2–50 keV band for the oscillation-med and low states, since the GSO data in these states have limited statistics due to the low flux and short exposure. The data of XIS-1, operated with the 0.1 s burst option, is almost free from pile-up effects and we can utilize all photons in the point spread function. Thanks to this fact, we can best estimate the continuum below 10 keV with least uncertainties in the calibration of the energy response of the XIS+XRT system, although the photon statistics is poorer than the data of the three FI-XISs. The observed spectra of the XIS-1 and HXD in the stable and oscillation state are plotted in Figure 3 (a) and (b), respectively.

Since the determination of the local features affects that of the continuum and vice versa, the above two steps are repeated in an iterative way. Firstly, we roughly determine the continuum shape from the BI-XIS and HXD spectra. Secondly, using the FI-XISs spectra in the 5–10 keV band, we determine local iron-K features, including absorption lines and an iron-K emission line, which is modelled by a feature from a reflection component. In this stage, we fix the parameters of the continuum at the best-fit obtained above except for its normalization. To take into account a remaining component of pile-up events, we add a power law component having a positive photon index in the model, whose parameters are set free. Thirdly, we again perform the continuum fit of the BI-XIS and HXD spectra, but including the reflection component and absorption line features, whose parameters are fixed at the best-fit values as determined in the previous fit of the FI-XISs spectra. Detailed description of the continuum model and local features is given in the following subsections.

#### 4.2. Absorption and Dust Scattering

In our study, special care is paid on two important effects

$5.8 \times 10^{22} \text{ cm}^{-2}$  for Si,  $7.6 \times 10^{22} \text{ cm}^{-2}$  for S, Cl, Ar, and Ca, and  $10 \times 10^{22} \text{ cm}^{-2}$  for Cr, Fe, Co, and Ni. The absorption cross section by Wilms et al. (2000) is adopted, which is available as *TBvarabs* model in XSPEC.

We also take into account the effects by dust scattering, which are more significant in soft X-rays particularly below  $\sim 3$  keV. A part of direct emission from a heavy absorbed source is scattered out by interstellar dust in the line-of-sight, while photons emitted with slightly different angles are scattered in, thus making dust-scattering halo around the target. At first order approximation the scattered-in and scattered-out lights cancel each other, although there is time delay before scattered-in components reach an observer following the direct component. Hence, we do need to correct for this effect as far as the source spectrum is constant *and* one can integrate all the emission including both direct and halo components.

This is not the case for GRS 1915+105 observed with *Suzaku*, however, because (1) the halo components cannot be fully collected in a limited field of view of the XIS and (2) the source is highly variable in the oscillation states. Assuming the same image profile of the dust scattered halo as GX 13+1 (Smith et al. 2002), which has a similar absorption column density to GRS 1915+105, we find that the effective area of the XIS-1 (full window) for the halo component is  $\approx 60\%$  of that for the direct (i.e., point source) one, and thus the scattering effect is not canceled out even when the spectrum is constant. When it is variable, the situation becomes more complex; the total spectrum observed in a given time interval is contaminated by halo components emitted in earlier epochs due to their time delay. The time scale of the delay is estimated to be  $\sim \theta^2 D/c$ , where  $\theta$  and  $D$  is the halo size and distance to the source, respectively. Taking  $\theta \sim 2'$  according to the halo profile of GX 13+1, we estimate the delay to be  $\sim 100$  hours, much longer than the time scale of the oscillations. This means that we approximately observe the spectrum of *variable* direct emission plus *constant* dust-scattered component in the oscillation states. According to the light curve of all sky monitor on *RXTE* (Ueda et al. 2006), the averaged flux level was almost constant for  $\sim 15$  days before our observation epoch, and thus we can reasonably assume that the shape of the direct spectrum producing the observed halo component is the same as that of the stable state.

To make the best estimate of the continuum spectra including low energies below  $\sim 3$  keV, we derive the spectrum of the halo component in the stable state, by taking into account the fact that 60% of the scattered-in component is contained in the observed spectrum. Here we refer to the cross section of dust scattering given by Draine (2003), which is fine-tuned to reproduce the observed halo intensity of GX 13+1 (Smith et al. 2002) at its hydrogen column density (Ueda et al. 2005). For the oscillation states, we subtract this component from the observed spectra and fit them by considering the opacity of both dust-scattering and photo-electric absorption. We assume that

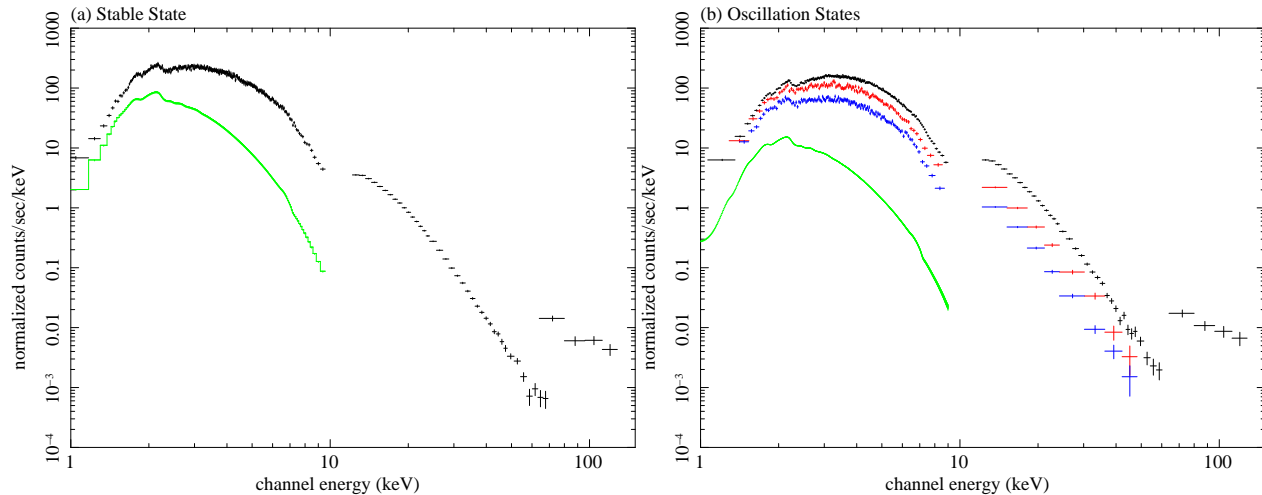


FIG. 3.— (a) (*left*) The observed spectra of XIS-1 (full window mode) and the HDX in the stable state, folded by the detector response. (b) (*right*) Those of XIS-1 (1/8 window mode) and the HDX in the oscillation-high (upper, black including the GSO), oscillation-med (middle, red), and oscillation-low (lower, blue) states. The lower curves in the XIS-1 band (green) indicate the estimated contribution of the dust scattered component.

The spectra of the FI-XISs with rich photon statistics reveal that the iron-K features are different between the four states. Figure 4 shows the summed FI-XISs spectra in the 5–10 keV band from which the estimated pile-up components (see above) are subtracted. The overlaid model is the best-fit continuum model with its reflection component, described below, from which both iron-K emission and absorption lines are excluded to show their significance; the ratio of the data to the model is plotted in the lower panel. In addition to a deep absorption-edge at 7.11 keV due to the overabundance of iron in the interstellar or circumstellar medium toward GRS 1915+105, we detect an emission line centered at 6.5–6.6 keV in both stable and oscillation low states, whereas it is very weak in the oscillation high and medium states. We also find a strong absorption line feature from He-like and H-like iron ions at  $\simeq 6.6$  and  $\simeq 7.0$  keV in the oscillation low state, which is weaker in the other states; in particular, no significant absorption lines are detected in the stable state.

We model the iron-K emission line by utilizing the *pexriv* reflection code (Magdziarz & Zdziarski 1995), which calculates both reflection continuum and fluorescence line. The line profile is further blurred with the *diskline* kernel (Fabian et al. 1989), by assuming that it originates from the accretion disk between the radii  $r_{\text{in}}$  and  $r_{\text{out}}$  with an emissivity law of  $r^\beta$ . The free parameters are (1) the solid angle of the reflector  $\Omega$ , which basically determines the equivalent width (EW) of the emission line, (2) ionization parameter  $\xi \equiv L/nr^2$  (Tarter et al. 1969) (where  $L$ ,  $n$ , and  $r$  is the luminosity, density of the reflector, and distance from the emitter, respectively), and (3) innermost radius  $r_{\text{in}}$ . We fix an iron abundance at the same value as in the interstellar absorption,

#### 4.4. Continuum Model

The overall shape of the continuum in the four states is characterized by a steep power law with a photon index of  $\approx 3$  at  $\sim 5$ –50 keV. To find an appropriate model to describe the continuum, we begin with fitting the XIS + HDX spectra in the 2–120 keV in the stable state, by taking into account the interstellar absorption and dust-scattering described in § 4.2, and the reflection component whose parameters are determined in the previous subsection. In addition, to include the opacity of the highly ionized gas responsible for the iron-K absorption lines, we introduce absorption edges at  $\approx 8.6$  keV and  $\approx 9.0$  keV corresponding to those by Fe XXV and Fe XXVI ions, respectively. We fix the optical depth according to the equivalent width of the corresponding absorption line (see Table 2), based on the results by Ueda et al. (2009). We first apply a canonical model consisting of a MCD component and a power law, which turns out to not acceptable ( $\chi^2/\text{dof} = 559/354$ ); moreover, the best-fit results are quite unphysical because (1) the innermost temperature of the MCD model is high ( $\sim 3$  keV) with an extreme small radius ( $\sim 4$  km) and (2) the power law component dominates the flux over the entire band. This confirms that the spectral state is very different from the canonical high/soft state of black hole binaries. Similar fitting results are reported by Munro et al. (1999) from *RXTE*/PCA data of GRS 1915+105 when the 0.5–10 Hz QPOs are observed.

Next, we apply a thermal Comptonization model by Życki, Done, & Smith (1999) with seed photons from a MCD component, as adopted by Done et al. (2004), Ueda et al. (2009), and Vierdayanti et al. (2009). By considering that a part of the MCD photons can escape without being Comp-

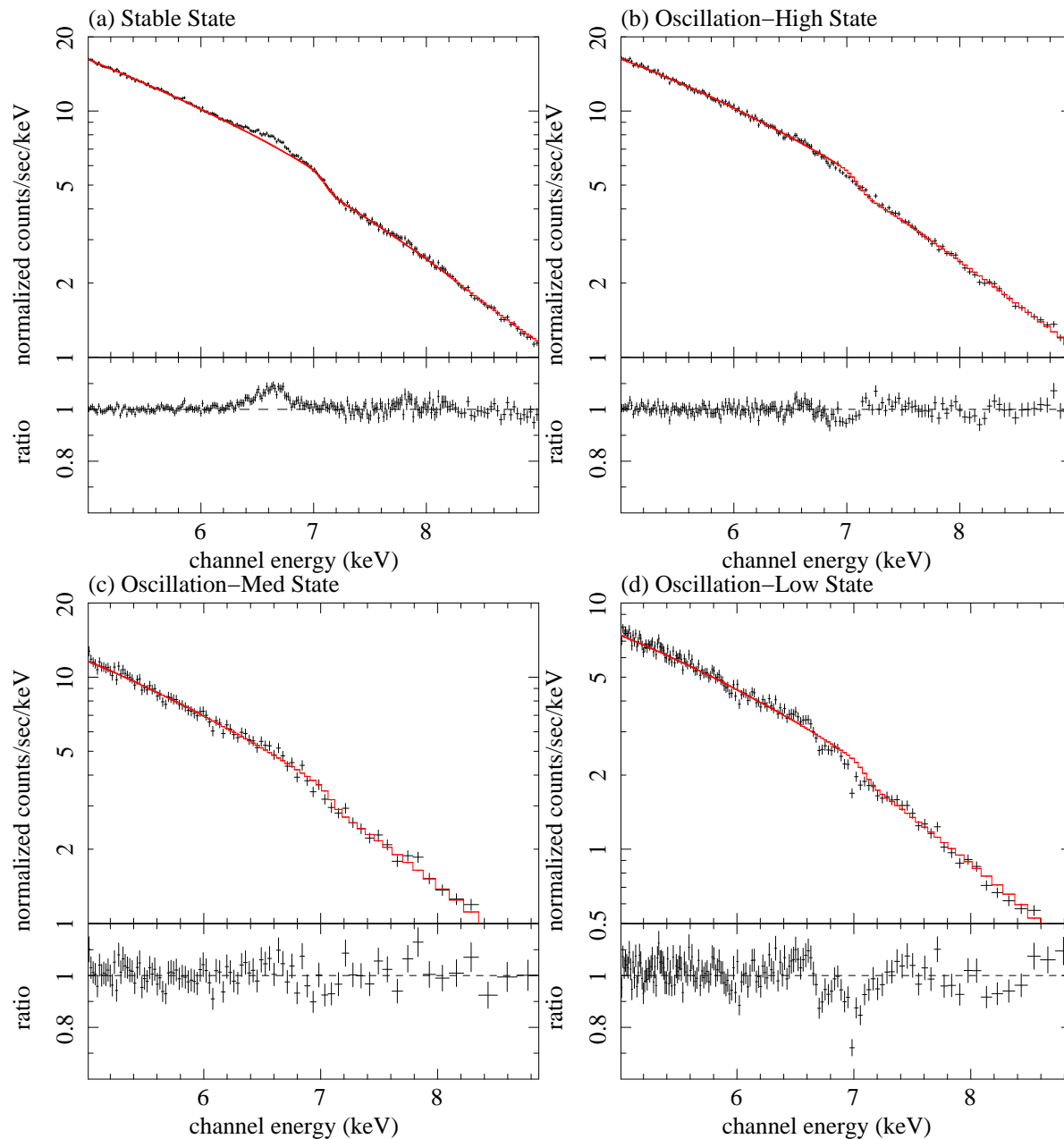


FIG. 4.— The FI-XISs spectra in the 5–10 keV band. The solid curves (red) represent the best-fit continuum model from which an iron-K emission and absorption lines are excluded. The lower panel plots the residuals in units of ratio between the data and above model. From left to right and top to bottom, (a) stable, (b) oscillation-high, (c) oscillation-med, and (d) oscillation-low state.

from the broad band spectra in the stable state. This result indicates that the spectrum can basically be represented with Comptonization of disk photons both by thermal and non-thermal electrons. The power-law description of non-thermal

energy input of accelerated electrons in a background thermal plasma. The model parameters are (1) the optical depth for scattering  $\tau$ , (2) compactness parameters, defined as  $l_{h,s} \equiv L_{h,s} \sigma_T / (Rm \cdot c^3)$ , where  $L_{h,s}$  is a power supplied to the plasma

TABLE 2  
SPECTRAL PARAMETERS

Parameters	Stable	Osc-H	Osc-M	Osc-L
Column Densities <sup>a</sup> ( $N_{\text{H}}$ )				
H ( $10^{22}$ cm <sup>-2</sup> )		2.78		
Mg ( $10^{22}$ cm <sup>-2</sup> )		6.3		
Si ( $10^{22}$ cm <sup>-2</sup> )		5.8		
S ( $10^{22}$ cm <sup>-2</sup> )		7.6		
Fe ( $10^{22}$ cm <sup>-2</sup> )		10		
Continuum <sup>b</sup>				
$T_{\text{in}}$ (keV)	0.53±0.04	0.79 <sup>+0.02</sup> <sub>-0.04</sub>	0.57±0.16	0.49 <sup>+0.14</sup> <sub>-0.19</sub>
( $T_{\text{e}}$ (keV))	2.2 <sup>+0.0</sup> <sub>-0.2</sub>	2.8 <sup>+0.0</sup> <sub>-0.2</sub>	1.7 <sup>+0.4</sup>	1.8 <sup>+0.3</sup>
$l_{\text{h}}/l_{\text{s}}$	0.94 <sup>+0.04</sup> <sub>-0.02</sub>	0.84 <sup>+0.02</sup> <sub>-0.05</sub>	0.69 <sup>+0.10</sup> <sub>-0.07</sub>	0.75 <sup>+0.16</sup> <sub>-0.07</sub>
$l_{\text{nt}}/l_{\text{h}}$	0.55±0.02	0.39 <sup>+0.04</sup> <sub>-0.01</sub>	0.34±0.09	0.17±0.05
$\tau$	8.3±0.3	7.5 <sup>+0.5</sup> <sub>-0.1</sub>	10 <sub>-1.7</sub>	10 <sub>-1.1</sub>
$\Gamma_{\text{inj}}$	3.7±0.2	3.1±0.3	3.1 (fixed)	3.1 (fixed)
$R_{\text{in}}^{\text{MCD}}$ (km) <sup>c</sup>	300 <sup>+50</sup> <sub>-30</sub>	120 <sup>+10</sup> <sub>-10</sub>	150 <sup>+50</sup> <sub>-150</sub>	190 <sup>+160</sup> <sub>-190</sub>
$R_{\text{in}}^{\text{total}}$ (km) <sup>d</sup>	420 <sup>+60</sup> <sub>-30</sub>	210 <sup>+20</sup> <sub>-10</sub>	360 <sup>+20</sup> <sub>-130</sub>	390 <sup>+380</sup> <sub>-160</sub>
Reflection <sup>e</sup>				
$\Omega/(2\pi)$	0.11±0.02	< 0.02	0.10±0.07	0.54 <sup>+0.06</sup> <sub>-0.07</sub>
$\xi$	530 <sup>+960</sup> <sub>-150</sub>	120 (fixed)	100 <sup>+360</sup> <sub>-60</sub>	39 <sup>+10</sup> <sub>-6</sub>
$r_{\text{in}}$ ( $r_{\text{g}}$ )	1000 <sub>-200</sub>	290(fixed)	290(fixed)	290 <sup>+170</sup> <sub>-140</sub>
(E.W.) <sup>f</sup> (eV)	33	<4	13	42
Iron-K Absorption Features				
$E_{\text{cen}}$ (keV)				6.76±0.33
E.W. (-eV)				26 <sup>+7</sup> <sub>-5</sub>
$E_{\text{cen}}$ (keV)	6.99 (fixed)	6.99 <sup>+0.02</sup> <sub>-0.05</sub>	7.01±0.10	7.02±0.02
E.W. (-eV)	<0.9	10.1 <sup>+2.7</sup> <sub>-2.4</sub>	15 <sup>+8</sup> <sub>-9</sub>	39 <sup>+5</sup> <sub>-8</sub>
$\tau_{8.6}^{\text{edge}}$	0	0	0	0.11
$\tau_{9.0}^{\text{edge}}$	0	0.051	0.072	0.20
Luminosity and Flux				
$L_{0.01-100}^{\text{MCD}}$ ( $10^{38}$ erg s <sup>-1</sup> )	9.2	7.6	3.0	2.8
$L_{0.01-100}^{\text{eqpair}}$ ( $10^{38}$ erg s <sup>-1</sup> )	10.4	15.2	14.4	8.8
$F_{2-10}^{\text{h}}$ ( $10^{-8}$ erg cm <sup>-2</sup> s <sup>-1</sup> )	1.69	2.88	1.92	1.12
$F_{10-50}^{\text{h}}$ ( $10^{-8}$ erg cm <sup>-2</sup> s <sup>-1</sup> )	0.63	1.03	0.39	0.17
Fitting Information				
Energy Range (keV)	2–120	2–120	2–50	2–50
$\chi^2 / \text{d.o.f}$	319/351	890/930	114/101	127/128

NOTE. — The errors are 90% confidence level for a single parameter.

<sup>a</sup> Equivalent hydrogen column densities as determined by Ueda et al. (2009), in units of Solar abundances (Anders & Grevesse 1989) between the element and hydrogen. The abundance ratios within each group of H-He-C-N-O, Ne-Na-Mg-Al, S-Cl-Ar-Ca, and Cr-Fe-Co-Ni are fixed at the Solar values.

<sup>b</sup> Fit with *eqpair* with a MCD spectrum as seed photons (see text). The compactness parameter for the seed photons is assumed to be  $l_{\text{s}} = 1000$ . Non-thermal electrons are considered between  $\gamma_{\text{min}} = 1.3$  and  $\gamma_{\text{max}} = 1000$  with a power law index of  $\Gamma_{\text{inj}}$ .

<sup>c</sup> The normalization of the directly observed MCD component in terms of

We find the *eqpair* + *diskbb* model, with the reflection of the former component, provides an excellent description of the continuum in all four states. The direct MCD component is required in the stable and oscillation-high states with the F-test probability of  $7 \times 10^{-3}$  and  $3 \times 10^{-8}$ , respectively. Although it is not significant in the oscillation-med and low states, we include this component for consistency. Figure 5 plot the unfolded spectra in units of  $EI(E)$ , where  $I(E)$  is the energy flux. The Comptonized component, MCD model, and the reflection component including the iron-K emission line, are separately plotted. The best-fit continuum parameters are summarized in Table 2, together with the observed 2–10 keV and 10–50 keV fluxes and absorption-corrected 0.01–100 keV luminosities for the Comptonization and MCD component, where a spherical and disk geometry is assumed, respectively. For the oscillation med and low states, we fix  $\Gamma_{\text{inj}} = 3.1$ , the best-fit value obtained in the oscillation high state, since it is difficult to constrain the slope without the coverage above 50 keV in these states.

## 5. DISCUSSION

### 5.1. Results Summary

With *Suzaku*, we obtained high quality broad band X-ray spectra of GRS 1915+105 over the 2–120 keV band both in the stable (Class  $\chi$ ) and oscillation states (Class  $\theta$ ), covered with CCD energy resolution (FWHM  $\sim 120$  eV at 6 keV) below 10 keV. The best estimated interstellar absorption and dust scattering effects are taken into account in the spectral fitting, which have been ignored in most of previous studies of GRS 1915+105. In particular, we caution that without correct modeling of the absorption with over iron abundances, one can easily reach wrong conclusions on the iron-K emission line profile that requires very careful analysis of the continuum shape. The best-fit models in units of  $EI(E)$  corrected for the interstellar absorption and scattering are plotted in Figure 6 for the four states. Below, we interpret our results based on the iron-K features and continuum model. We find that the iron-K features in the oscillation low state are very similar to those in the “soft state” (steady State A) of GRS 1915+105 detected by Ueda et al. (2009) using *Chandra*/HETGS. This may be expected, since our oscillation low state mostly corresponds to State A, though not in a steady state.

### 5.2. Change of Reflection

We detect significant iron-K emission lines, direct evidence for the reflection, in the stable, oscillation-med, and oscillation-low states. The line profiles indicate that the reflector is moderately ionized ( $\log \xi \sim 1-3$ ) and is located far away from the black hole as constrained by its “narrow” line width; it is most probably the outer parts of the accretion disk, whose inner radius is estimated to be  $\gtrsim 300r_{\text{g}}$  by assuming an emissivity law of  $r^{-3}$ . This does not mean that the disk must

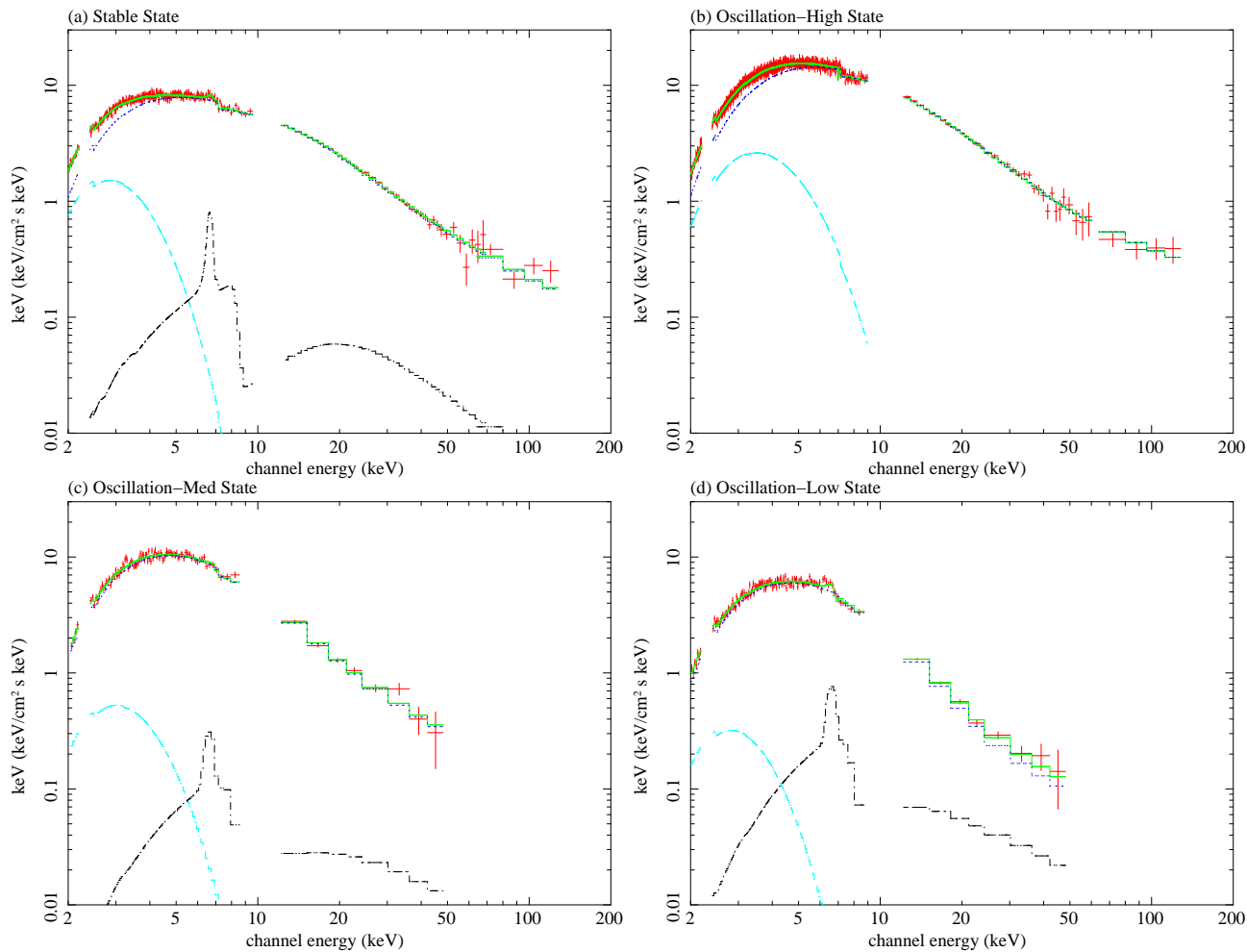
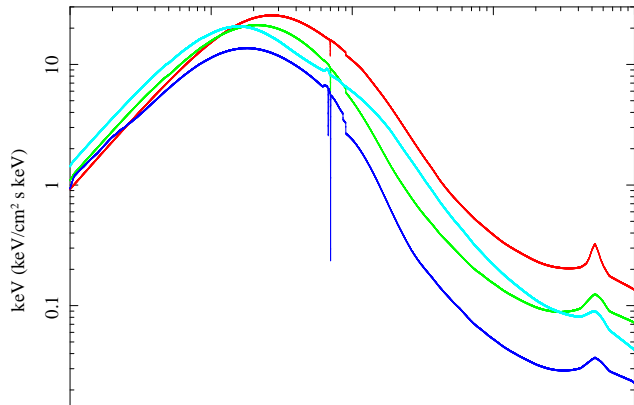


FIG. 5.— The unfolded spectra in units of  $E I(E)$  obtained from the XIS-1 and HXD data (red, crosses) plotted with separate contribution of the model; from upper to lower, the total (solid, green), Comptonized component (dot, blue), direct MCD component (dash, cyan), and reflection component (dot-dash, black). From left to right and top to bottom, (a) stable, (b) oscillation-high, (c) oscillation-med, and (d) oscillation-low state.



attribute this change mainly to the variability in the solid angle of the reflector as seen by the central source. In the stable state, the solid angle is small  $\Omega/2\pi \approx 0.1$  as well, similar to that found in the oscillation med state.

We interpret that this is the first observational evidence for “self-shielding” effects of the inner part of the accretion disk. The dynamical structure of outer parts of the accretion disk,  $r \gtrsim 300r_g$ , cannot be changed on a time scale of the limit-cycle,  $\sim 1000$  sec, much shorter than that of viscosity (Shakura & Sunyaev 1973). Therefore, the only possible mechanism that can dramatically reduce the observed reflection strength in the oscillation-high state must be related to the geometry in the central source; most of the continuum X-ray emission seen by an observer (i.e., with  $i = 70^\circ$ ) does not reach



### 5.3. Disk Wind

As have been revealed by previous studies (Kotani et al. 2000; Lee et al. 2002; Ueda et al. 2009; Neilsen & Lee 2009), absorption lines of highly ionized ions indicate the presence of a disk wind in the line-of-sight between the continuum emitter and the observer. The disk wind has a velocity of  $v_{\text{wind}} \approx 500 \text{ km s}^{-1}$  and is most likely launched at outer parts of the disk,  $r_{\text{wind}} \sim 10^5 r_g$  (Ueda et al. 2009), by irradiation from the central source. During the limit cycle, the absorption lines are the deepest in the oscillation-low state and become weaker as the hard X-ray flux increases. This strongly supports the photoionization of the wind; the corresponding ionization parameters estimated from the population ratio between Fe XXVI and Fe XXV are consistent with the change of the luminosity (based on an XSTAR simulation; Kallman 2003). The self-shielding is not relevant for photo-ionization, as the wind we observe is located  $20^\circ$  above the disk plane. The wind is most probably developed by the strong X-ray irradiation in the oscillation-low state, as indicated by its strong iron-K emission line. Once a disk wind is launched, it will travel over a time scale of  $r_{\text{wind}}/v_{\text{wind}} \sim 10^4$  sec, and hence we can approximate that the same disk wind steadily exists during the limit cycles.

In the stable state, we do not detect any iron-K absorption lines. This suggests three possibilities; (1) the wind is not developed, (2) the wind is fully ionized, or (3) the scale height of the disk wind is too low to be observed. We consider the first possibility unlikely because the absorption lines have been detected in the same Class  $\chi$  state even when the hard X-ray flux is lower than in our observation (Lee et al. 2002). Indeed, the presence of iron-K emission line suggests that illumination of the outer parts of the disk does occur, which can trigger the launch of the wind. The second possibility cannot be ruled out, if the density of the wind is much smaller than that develops in the oscillation states. Then, the ionization parameter may become sufficiently large to be fully ionized, even if the luminosity is smaller than that in the oscillation-high state. The third possibility is also plausible.

### 5.4. Origin of the Continuum

We have shown that the broad band spectra in all the four states can be commonly explained by Comptonization of seed disk photons off optically-thick ( $\tau \approx 7-10$ ), low temperature ( $T_e \approx 2-3 \text{ keV}$ ), non-thermal hybrid plasmas. Similar results are obtained by Zdziarski et al. (2001) in another state of GRS 1915+105 (Class  $\gamma$  or State B). These findings indicate that the optically thick and low temperature Comptonization are common features in accretion flows at high Eddington fractions, as suggested by Done et al. (2004) and Ueda et al. (2009). In the stable and oscillation-high states, we find that the fractional power supplied to non-thermal electrons is quite large ( $l_{\text{nt}}/l_{\text{h}} = 0.4-0.6$ ) and the slope of the

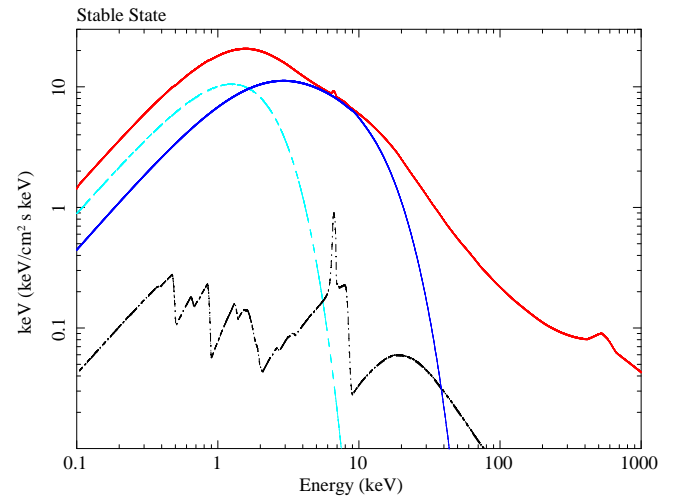


FIG. 7.— The  $EI(E)$  spectrum in the stable state corrected for the interstellar absorption and dust-scattering. The thick solid curve (red) represents the total, the dashed curve (cyan) the direct MCD component, the dot-dashed curve (black) the reflection component, and the thin solid curve (blue) thermal Comptonization component that would be observed without non-thermal electrons.

in the stable and oscillation-high states, assuming the same temperature for the seed photons and MCD component. This implies that (Case I) the Comptonizing plasmas are patchy over the disk, or (Case II) they are located inside a “truncation radius” of the standard disk. In reality, such truncation would be smooth; the disk may gradually change into the “disk+corona” region, as suggested for the very high state of canonical black hole binaries (e.g., Done & Kubota 2006). In Case II, the assumption of the same spectrum for the direct MCD and seed photons do not hold, and a disk radius derived from such a simple model may be largely overestimated from the true disk size if the energetics coupling between the disk and corona is taken into account (Done & Kubota 2006).

From the observed flux and innermost temperature obtained from the fit, we can estimate the innermost radius of the accretion disk both for the direct MCD component ( $R_{\text{in}}^{\text{MCD}}$ ) and that of the seed photons for the Comptonized component ( $R_{\text{in}}^{\text{Comp}}$ ). We calculate  $R_{\text{in}}^{\text{Comp}}$  by assuming the conservation of photon numbers in the Comptonization process, according to the formula (A1) of Kubota & Makishima (2004) with the left-hand term increased by a factor of two for the optically thick case. The resultant values of  $R_{\text{in}}^{\text{MCD}}$  and  $R_{\text{in}}^{\text{total}} =$

$\sqrt{(R_{\text{in}}^{\text{MCD}})^2 + (R_{\text{in}}^{\text{Comp}})^2}$  are listed in Table 2, without any corrections for the boundary condition and color/effective temperature, which would increase the radius by a factor of  $\approx 1.2$  (Kubota et al. 1998). In Case I,  $R_{\text{in}}^{\text{total}}$  corresponds to the true innermost radius corrected for the partial coverage by Comptonization.

ting (e.g., Belloni et al. 1997b; Migliari & Belloni 2003), although we obtain larger radii than these studies that refer only to the MCD component by ignoring Comptonized photons. In the stable state, the radius ( $R_{\text{in}}^{\text{total}} \approx 420$  km) is significantly larger than that in the oscillation-high state. Thus, if Case I is true, our results suggest that the standard disk does not extend down to the innermost stable circular orbit (ISCO) regardless of the black hole spin in all our states, unlike in some cases of the “soft state” of GRS 1915+105 (McClintock et al. 2006; Middleton et al. 2006; Vierdayanti et al. 2009). Such low-temperature/high-luminosity disk emission that leads to an apparently large disk radius is observed in the very high state of other black hole binaries (Done & Kubota 2006), when the Eddington ratio is higher than that in the high/soft state. At even higher Eddington fractions that trigger limit cycles, as in our case, the situation may be the same as in the canonical very high state.

The Comptonization parameters also show significant change during the limit-cycle oscillation, besides the disk radius (and disk temperature) as discussed above. In the oscillation high state, the fractional power supplied to non-thermal electrons becomes the largest ( $l_{\text{nt}}/l_{\text{h}} \approx 0.4$ ) and the electron temperature highest ( $T_{\text{e}} = 2.8$  keV), which decreases to  $l_{\text{nt}}/l_{\text{h}} \approx 0.2$  and  $T_{\text{e}} = 1.8$  keV in the oscillation-low state, respectively. Thus, in the flare phase, very efficient particle acceleration must occur by converting the gravitational energy of accreting mass. This may increase the temperature of thermal electrons and expand the size of the corona. As the corona becomes geometrically thick, the “self-shielding” effect starts to work, preventing the Comptonized photons from irradiating the outer part of the accretion disk (i.e., little reflection signals). A similar situation (geometrically thick corona) may be realized in the stable state as well, where the reflection strength is weaker compared with the oscillation low states.

To summarize, with the simple spectra model presented above, we show that the dramatic change of X-ray flux and spectra during the limit-cycle oscillation can be explained mainly by (1) the evolution of the disk geometry and (2) that of physical parameters of Comptonizing corona, particularly the fractional power supplied to non-thermal electrons. We note, however, that the assumption of the MCD model (i.e., standard disk) in all states and that of the same temperature for the seed photons of Comptonization would be oversimplification. For instance, disk instability theories predict that a slim disk appears in the oscillation high state (Abramowicz et al. 1988), which predicts different spectra from the MCD model. This is not ruled out from the current simple analysis. Nevertheless, we stress that the role of Comptonization becomes very important in determining the whole dynamics and energy spectra of black hole accretion disks at high mass accretion rates, which must be taken into account in any theoretical studies.

## 6. CONCLUSIONS

1. We find that the *Suzaku* broad band spectra of GRS 1915+105 band both in the stable (Class  $\chi$ ) and oscillation states (Class  $\theta$ ) are commonly represented with a model consisting of a MCD model and its Comptonization with a reflection component, over which the opacity of the disk wind (including iron-K absorption lines) is applied. The Comptonized component dominates the flux above  $\sim 3$  keV.
2. The Comptonization is made by optically-thick ( $\tau \approx 7-10$ ), non-thermal / thermal ( $T \approx 2-3$  keV) hybrid plasmas. The non-thermal electrons are produced with 10–60% of the total energy input to the plasma with a power law index of  $\approx 3-4$ , which account for the hard X-ray tail above  $\sim 50$  keV.
3. During the limit-cycle oscillation, the reflection strength, estimated by the iron-K emission line, is the largest during the dip phase but disappears in the flare phase. We interpret this as evidence for self-shielding effects that Comptonized photons are obscured by the surrounding cool region of the expanded disk when viewed at a very high inclination angle from the outer disk. The evolution of the disk geometry is in accordance with theoretical predictions.
4. The disk wind, traced by iron-K absorption lines of Fe XXV and Fe XXVI, always exists during the oscillation and its ionization well correlates with the X-ray flux. This supports the photoionization origin. In the stable state, the iron-K absorption lines are not detected probably because it is highly ionized and/or the scale height is small.
5. The disk parameters suggest that the inner disk structure is similar to that in the very high state of black hole binaries. The spectral variability in the oscillation state is explained by the change of the disk geometry and of physical parameters of Comptonizing corona, particularly the fractional power supplied to the acceleration of non-thermal particles.

We thank the *Suzaku* team and 2005 October multiwavelength campaign team, for enabling us to perform these observations as a *Suzaku* SWG program. Part of this work was financially supported by Grants-in-Aid for Scientific Research 20540230, and by the grant-in-aid for the Global COE Program “The Next Generation of Physics, Spun from Universality and Emergence” from the Ministry of Education, Culture, Sports, Science and Technology (MEXT) of Japan.

- Greiner, J., Cuby, J.G., & McCaughrean, M.J., 2001, *Nature*, 414, 522
- Homan, J. & Belloni, T. 2005, *Ap&SS*, 300, 107
- Kubota, A., Tanaka, Y., Makishima, K., Ueda, Y., Dotani, T., Inoue, H., Yamaoka, K. 1998, *PASJ*, 50, 667
- Kubota, A. & Makishima, K. 2004, *ApJ*, 601, 428
- Fabian, A.C., Rees, M.J., Stella, L., White, N.E. 1989, *MNRAS*, 238, 729
- Kallman, T.R. 2003, *XSTAR User's Guide Version 2.1j*, [ftp://legacy.gsfc.nasa.gov/software/plasma\\_codes/xstar](ftp://legacy.gsfc.nasa.gov/software/plasma_codes/xstar)
- Kotani, T., Ebisawa, K., Dotani, T., Inoue, H., Nagase, F., Tanaka, Y., Ueda, Y. 2000, *ApJ*, 539, 413
- Lee, J.C., Reynolds, C.S., Remillard, R., Schulz, N.S., Blackman, E.G., Fabian, A.C. 2002, *ApJ*, 567, 1102
- Magdziarz, P. & Zdziarski, A. A. 1995, *MNRAS*, 273, 837
- McClintock, J. E., Shafee, R., Narayan, R., Remillard, R. A., Davis, S. W., & Li, L.-X. 2006, *ApJ*, 652, 518
- Middleton, M., Done, C., Gierliński, M. Davis, S.W. 2006, *MNRAS*, 373, 1004
- Middleton, M., Done, C., Ward, M., Gierliński, M., Schurch, N. 2009, *MNRAS*, 394, 250
- Migliari, S. & Belloni, T. 2003, *A&A*, 404, 283
- Mirabel, I.F. & Rodríguez, L.F. 1994, *Nature*, 371, 46
- Mitsuda, K., et al. 1984, *PASJ*, 36, 741
- Mitsuda, K., et al. 2007, *PASJ*, 59S, 1
- Muno, M., Morgan, E., Remillard, R. 1999, *ApJ*, 527, 321
- Neilsen, J. & Lee, J.C. 2009, *Nature*, 458, 481
- Ohsuga, K. 2006, *ApJ*, 640, 923
- Reig, P., Belloni, T., van der Klis, M. 2003, *A&A*, 412, 229
- Remillard, R. A. & McClintock, J. E. 2006 *ARA&A*, 44, 49
- Rodriguez, J. et al. 2008a, *ApJ*, 675, 1436
- Rodriguez, J. et al. 2008b, *ApJ*, 675, 1449
- Shakura, N.I., & Sunyaev, R.A. 1973, *A&A*, 24, 337
- Tanaka, Y., & Lewin, W.H.G. 1995, in *X-Ray Binaries*, ed. W.H.G. Lewin, J. van Paradijs, & E.P.J. van den Heuvel (Cambridge: Cambridge Univ. Press), 126
- Tarter C.B., Tucker W., Salpeter E.E. 1969, *ApJ*, 156, 943
- Smith, R.K., Edgar, R.J., Shafer, R.A. 2002, *ApJ*, 581, 562
- Ueda, Y., Mitsuda, K., Murakami, H., Matsushita, K. 2005, *ApJ*, 620, 274
- Ueda, Y., et al. 2009, in *Proc. VI Microquasar Workshop: Microquasars and Beyond*, ed. T. Belloni (Como: Proc. Science), 23.1
- Ueda, Y., Yamaoka, K., Remillard, R. 2009, *ApJ*, 695, 888
- Vierdayanti, K., Mineshige, S., Ueda, Y. 2009, *PASJ*, in press (arXiv:1001.3906)
- Wilms, J., Allen, A., McCray, R. 2000, *ApJ*, 542, 914
- Życki, P. T., Done, C., Smith, D.A. 1999, *MNRAS*, 309, 561
- Zdziarski, A.A., Grove, J.E., Poutanen, J., Rao, A.R., Vadawale, S.V. 2001, *ApJ*, 554, L45
- Zdziarski, A.A., Gierliński, M., Rao, A.R., Vadawale, S.V., Mikolajewska, J. 2005, *MNRAS*, 360, 825